

Thermally-Activated Epitaxy of NbO

Sandra Glotzer,^{1,2} Jeong Rae Kim,^{1,2} and Joseph Falson^{1,2,*}

¹*Department of Applied Physics and Materials Science,
California Institute of Technology, Pasadena, California 91125, USA.*

²*Institute for Quantum Information and Matter,
California Institute of Technology, Pasadena, California 91125, USA.*

Abstract

We demonstrate a thermally-activated epitaxy window for the growth of NbO at temperatures exceeding 1000 °C. NbO films grown in this mode display superior structural and transport properties, which are reproducible across a window of oxygen partial pressure. Through comprehensive analysis, we propose the prototypical electrical properties of NbO, for which a consensus has not yet been made. This study unequivocally demonstrates the utility of high temperatures in the thin film synthesis of refractory metal compounds.

I. INTRODUCTION

The interplay between electron correlations and strong spin-orbit coupling (SOC) has resulted in a variety of emergent quantum phenomena and topological phases [1]. Among prevailing material platforms, the 4d and 5d transition metal systems are ripe hosts for these effects, as SOC is a competing and comparable energy scale to kinetic energy. Some prominent examples in this correlated SOC regime include the 2D transition metal dichalcogenides [2], Weyl semimetal pnictides [3, 4], and iridates [1, 5], some of which have hosted novel transport phenomena, such as extremely large nonsaturating magnetoresistance [6, 7] and chiral anomaly induced negative longitudinal magnetoresistance [8, 9]. However, these transport signatures can be obscured or complicated by extrinsic effects due to material imperfections or geometric configuration, such as weak localization [10], current jetting [11–13], and ionic impurity induced scattering [14]. Therefore, a thorough understanding of the mechanisms behind these interesting transport features and the synthesis conditions for reproducible, high-quality crystals, is essential.

NbO, one such transition metal compound, is a highly metallic 4d³ system and was among the first oxide superconductors discovered ($T_c = 1.61$ K) [15–17]. NbO_{1+x} forms in a unique vacancy-ordered rock-salt structure with 25% vacancies on each sublattice [18], and it exists over a very narrow homogeneity range ($-0.02 \leq x \leq 0.02$) [15, 17], making it a controlled system for studying the influence of oxygen vacancy concentration and band filling on electrical transport properties. It has a complex band structure, with electrons and holes in several bands contributing to the transport properties [19–22]. In bulk crystals, the trans-

* falson@caltech.edu

port properties were found to vary significantly with small changes in NbO_{1+x} composition [23, 24], but there are many discrepancies between reports in terms of the magnitudes and trends, making interpretation difficult. These discrepancies can be attributed to impurities and the difficulty of precisely controlling and accurately determining the stoichiometry.

In this work, we report the correlation between growth conditions and transport properties of NbO thin films in the oxygen partial pressure (P_{O_2}) and growth temperature (T_{G}) phase space. At high growth temperatures ($T_{\text{G}} > 1000$ °C), accessible via laser heating, we observe a thermally-activated epitaxy window that yields sharp boundaries between NbO and its proximate phases, Nb and NbO_2 . In this growth regime, we find superior crystal quality and transport properties, which are reproducible across a wide P_{O_2} window. We propose the prototypical electrical properties, namely the temperature dependence of the Hall coefficient (R_{H}) and the superconducting transition temperature (T_{c}), of NbO, for which a consensus has not yet been made.

II. METHODS

Nb-O films were prepared on Al_2O_3 (0001) substrates using a molecular beam epitaxy system equipped with a CO_2 laser heating apparatus. Al_2O_3 (0001) was previously determined to be the most suitable substrate on which to grow NbO (111), despite the large lattice mismatch of -7.7% [25]. Prior to growth, the substrates were annealed at $T = 1500$ °C for 10 minutes to obtain atomically flat terraces. Using a similar growth recipe to Ref. [25], a Nb flux of approximately $10 \text{ ng/cm}^2 \cdot \text{s}$, as measured by a quartz crystal microbalance (QCM), was supplied by an electron beam evaporator. This flux resulted in an average NbO film thickness of ≈ 50 nm for a growth time of 1 hour. The flux was monitored during the growth using the QCM and the current supplied to the electron beam evaporator was adjusted to compensate for changes in Nb flux. Molecular oxygen was supplied using two variable leak valves in series with a baratron in between. The pressure in the intermediate volume was used as a tunable parameter. The corresponding chamber pressure using a nude ion gauge in the growth chamber ranged from 3×10^{-8} to 1×10^{-6} mbar for oxygen nozzle pressures of 0.05 to 0.40 mbar.

X-ray diffraction (XRD) analysis was performed using a Rigaku Smartlab diffractometer with a $\text{Cu}-K\alpha 1$ source. Reciprocal space mapping data was obtained using the Rigaku

HyPix 3000 1D detector.

Electrical properties were measured using a Quantum Design Dynacool Physical Property Measurement System equipped with a dilution refrigerator option. The samples were wire bonded in a Van der Pauw configuration using aluminum wires. Resistivity measurements were obtained using the internal resistance bridge of the Dynacool system at a current of 100 μA for normal state transport measurements and 10 μA for measurements in the dilution refrigerator.

III. RESULTS

A common theme among 4*d* and 5*d* compounds containing refractory metals is that the high melting points, which result from strong metallic bonding [26–28], create challenges when it comes to synthesis. Very high temperatures and significant time can be required in order for the metallic bonds to be broken and the elements to diffuse and react [29–31]. Therefore, it can be challenging to realize ideal thermal conditions for the growth of superior-quality crystals and, given the additional restrictions in the thin film deposition process, their epitaxial growth.

Before describing the experimental details of our study, we consider two synthesis aspects. First, we consider equilibrium thermodynamics, which predict monotonically stronger reducing conditions as T_{G} increases and P_{O_2} decreases [34]. To visualize this concept, we use the Ellingham diagram [35], which relies on the relation between the Gibbs free energy change (ΔG) and the equilibrium constant (K) under isobaric conditions,

$$\Delta G = \Delta G_0 + RT \ln K = \Delta G_0 - RT \ln a_{\text{O}_2}. \quad (1)$$

Here, ΔG_0 is the change in the standard Gibbs free energy, R is the gas constant, T is the absolute temperature, and a_{O_2} is the activity of oxygen. Second, we take into account kinetics, which is described by the Arrhenius equation. We have approximated the temperature-dependent reaction rate (K) for the oxidation of Nb as

$$K \approx C' \exp\left(\frac{-E_A}{RT}\right) P_{\text{O}_2} \quad (2)$$

where E_A , the activation energy, is obtained from previous literature as 71 kJ/mol [36], and the constant C' incorporates the Arrhenius factor and the activity of Nb, which is typically

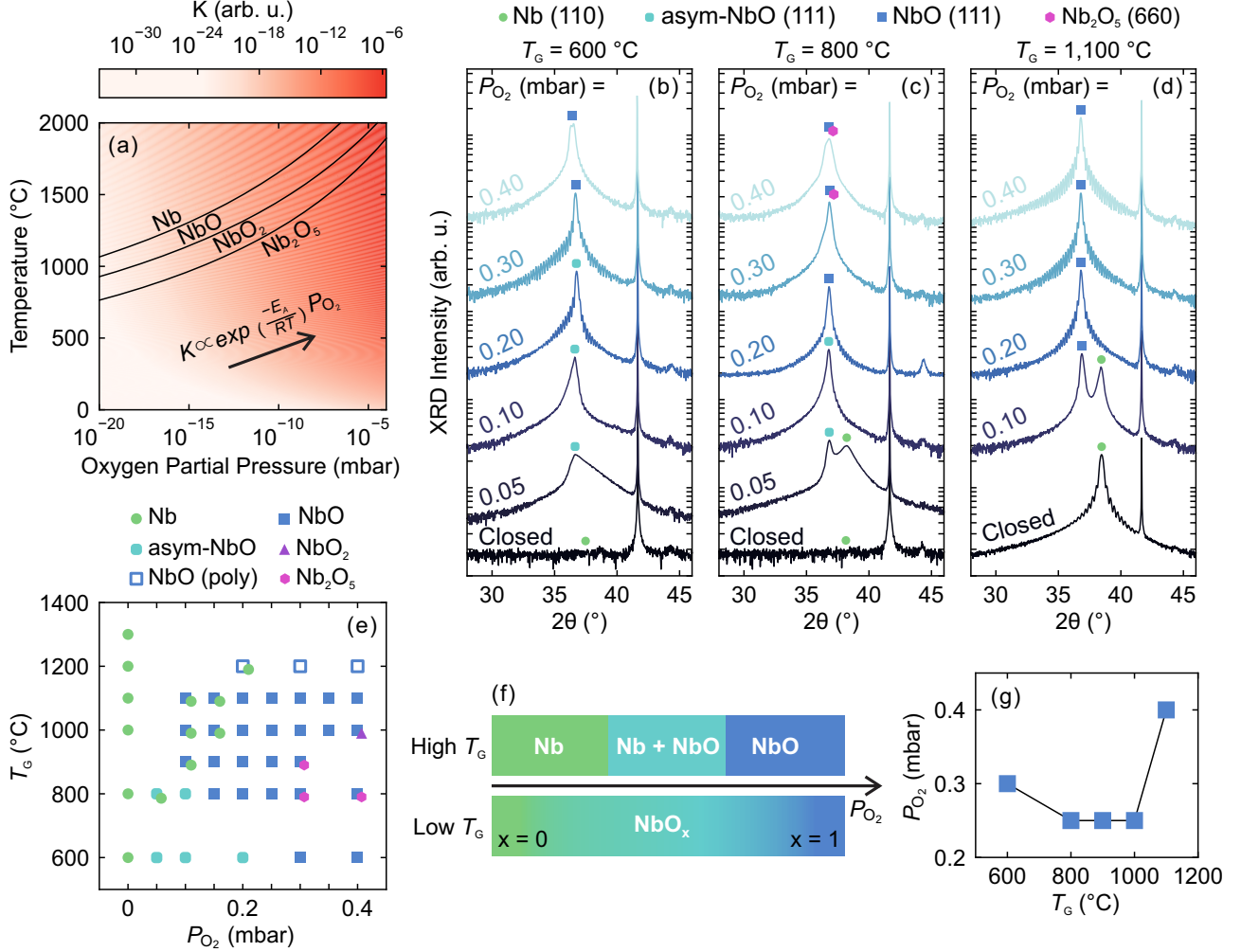


FIG. 1. Growth dynamics of the Nb-O system. (a) Kinetic and thermodynamic considerations for the formation of Nb oxides. The shaded contour plot represents the reaction rate (K) for the oxidation of Nb for various values of temperature and oxygen partial pressure. The black curves represent the Ellingham diagram for the formation of NbO, NbO₂, and Nb₂O₅ from the constituent elements. Thermodynamic data have been taken from Refs. [32, 33] using standard conditions. (b-d) XRD 2θ-ω scans of Nb-O films grown at $T_G = 600$, 800 and 1100 °C with varying P_{O_2} . (e) Growth phase diagram of Nb-O on Al₂O₃ (0001) in the T_G - P_{O_2} parameter space. Symbols correspond to body-centered-cubic Nb (green circle), asymmetric NbO (cyan rounded square), polycrystalline NbO (open blue square), single-phase, single-crystal NbO (filled blue square), rutile NbO₂ (purple triangle), and Nb₂O₅ (pink hexagon). (f) Schematic illustrating the effect of T_G on the amount of phase separation between Nb and NbO. (g) Optimal P_{O_2} for forming the highest crystal quality NbO as a function of T_G .

unity for solids [34]. These thermodynamic and kinetic mechanisms are illustrated in Fig. 1(a). The black curves represent the Ellingham diagram for the oxidation of Nb, and the contour plot represents the reaction rate.

With these concepts in mind, we turn to the growth of the Nb-O thin film system. To control the oxidation state, we vary T_G and P_{O_2} while keeping all other parameters fixed. In Figs. 1(b-d) we show XRD $2\theta-\omega$ scans of Nb-O films grown at select T_G and varying P_{O_2} . At $T_G = 600$ °C [Fig. 1(b)], amorphous Nb forms when the oxygen nozzle is closed. When the nozzle is open, bad-quality NbO, as evidenced by the asymmetric NbO (111) peak, forms at low P_{O_2} ($P_{O_2} = 0.05$ - 0.20 mbar). High-quality, symmetric NbO with well-defined Laue oscillations forms at intermediate P_{O_2} ($P_{O_2} = 0.30$ mbar). Further increasing P_{O_2} to 0.40 mbar results in a slight splitting of the NbO (111) peak and a lack of Laue oscillations, indicating poor quality. At $T_G = 800$ °C [Fig. 1(c)], amorphous Nb again forms at P_{O_2} = “Closed”. As P_{O_2} is increased, the Nb-O system is progressively oxidized, transforming from bad-quality NbO mixed with Nb ($P_{O_2} = 0.05$ mbar), to asymmetric NbO ($P_{O_2} = 0.10$ mbar), to good-quality NbO ($P_{O_2} = 0.20$ mbar), to NbO mixed with an impurity phase which is challenging to conclusively determine, but which is likely Nb₂O₅ ($P_{O_2} = 0.30$ - 0.40 mbar) [Supplemental Material, Fig. S1]. At $T_G = 1100$ °C [Fig. 1(d)], high-quality, crystalline Nb forms at P_{O_2} = “Closed”, and opening the nozzle to low P_{O_2} ($P_{O_2} = 0.10$ mbar) yields NbO mixed with Nb, with sharp separation between the peaks. Further increasing P_{O_2} results in the formation of single-phase NbO with excellent crystal quality across a wide P_{O_2} window (0.20 - 0.40 mbar). The crystal quality improves with increasing P_{O_2} , as evidenced by the increasing intensity and range of the Laue oscillations.

It is difficult to identify a comprehensive trend from these three sample sets, so we explore the growth of Nb-O in an extended range of the P_{O_2} - T_G parameter space [Fig. 1(e)]. All P_{O_2} = “Closed” samples are Nb metal whose crystalline state evolves from amorphous to (110)-oriented as T_G increases. Above $T_G = 1100$ °C, NbO is polycrystalline, presumably due to entropy and the large lattice mismatch between NbO and Al₂O₃ (0001). The asymmetric NbO phase appearing in the low T_G and low P_{O_2} conditions is tentatively considered to be NbO with Nb defects [Fig. 1 (f)], which will be discussed in detail later. Progressive oxidation occurs for all T_G series with increasing P_{O_2} and, notably, higher oxidation states emerge only under intermediate T_G conditions. In a similar manner, a comparison of T_G -varied samples at fixed P_{O_2} (0.2, 0.3, and 0.4 mbar) suggests that the oxidation state increases and then

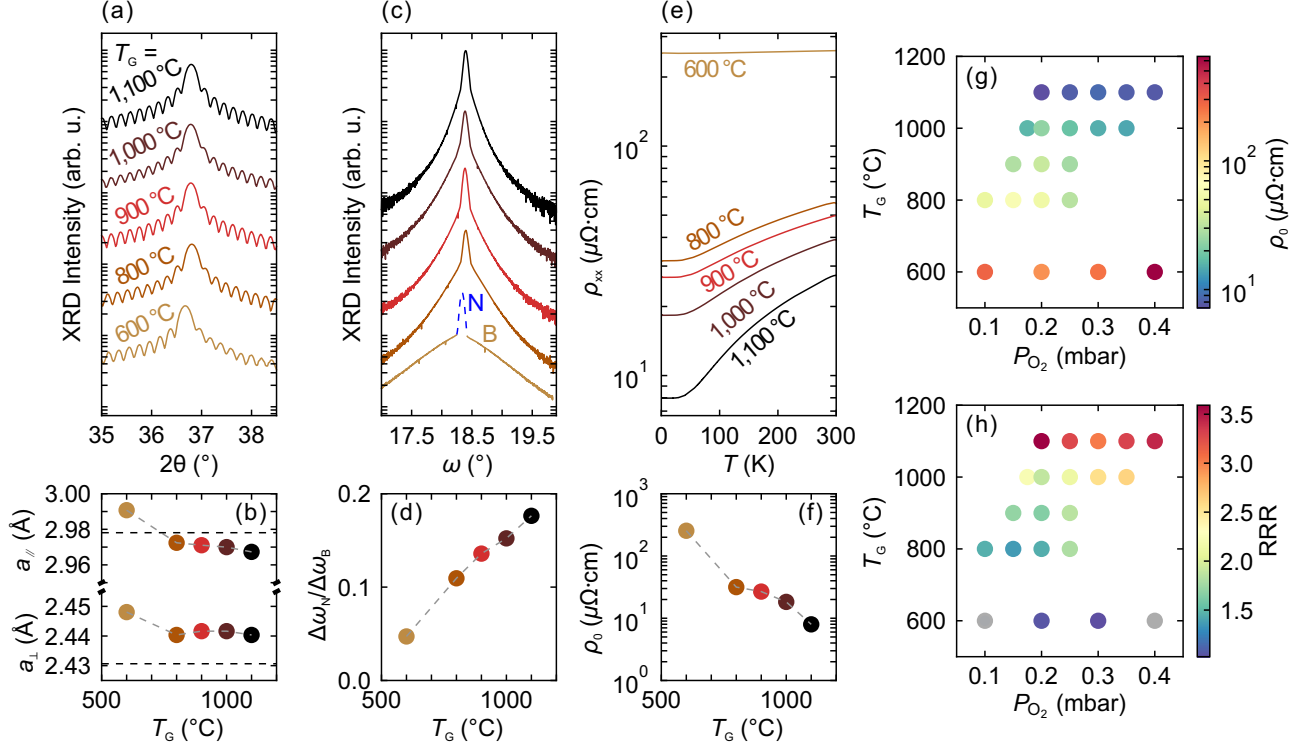


FIG. 2. Deterministic role of T_G on the structural and transport properties of NbO. (a) Narrow-range XRD 2θ - ω scans of NbO films grown at varying T_G and the corresponding optimal P_{O_2} . (b) (Top) in-plane [112] lattice constant ($a_{//}$) and (bottom) out-of-plane [111] lattice constant (a_{\perp}) of the same samples as a function of T_G . Black dashed lines correspond to the respective bulk NbO values. (c) Rocking curve measurements of the NbO (111) peak and (d) ratio of the full width at half maximum (FWHM) of the narrow component (N) to the FWHM of the broad component (B) of the rocking curves. The curves were fitting using a Gaussian function for the narrow component and a squared Lorentzian function for the broad component. (e) Temperature-dependent longitudinal resistivity and (f) residual resistivity (ρ_0) at 1.7 K of the same samples. (g) ρ_0 and (h) residual resistivity ratio (RRR) of NbO samples in the T_G - P_{O_2} parameter space. Gray circles represent insulating samples.

decreases as a function of T_G . This non-monotonic temperature dependence of oxidation can be qualitatively interpreted as a competition between the two trends discussed earlier. At low temperatures, NbO is stable up to high P_{O_2} , but it is rapidly oxidized with increasing temperature, in accord with the Arrhenius equation. At high temperatures, NbO becomes more reduced with increasing T_G and decreasing P_{O_2} , following Ellingham thermodynamics.

The growth temperature triggers a shift in the growth mode from kinetics-driven ($T_G \leq 900$ °C) to thermodynamics-driven ($T_G > 900$ °C), suggesting thermal activation of the Nb-O system. The crossover temperature from kinetics- to thermodynamics-driven appears to be closely correlated with evolution of the Nb crystalline state as well as the occurrence of the asymmetric NbO phase. In accord with the non-monotonic T_G -dependence of oxidation, the P_{O_2} for forming the highest crystal quality NbO varies non-monotonically with T_G , as shown in Fig. 1g). The “optimal” samples were selected by evaluating the NbO (111) peak shape and Laue oscillations for all growth conditions [Supplemental Material, Fig. S2], and while this is not physically rigorous, it will be used as a guide for discussions below.

Given the deterministic role of T_G in the epitaxial Nb-O system, we investigate its effects on the structural and transport properties of NbO. Fig. 2(a) shows narrow-range XRD 2θ - ω scans of NbO films grown at the optimal P_{O_2} [see Fig. 1(g)] for each T_G series. In Fig. 1(b), we plot the in-plane (a_{\parallel}) and out-of-plane (a_{\perp}) lattice constants, which are extracted from XRD analysis, as a function of T_G . Both a_{\parallel} and a_{\perp} are larger than the bulk values for the $T_G = 600$ °C sample, but the lattice constants rapidly decrease as T_G increases, resulting in a_{\parallel} being smaller and a_{\perp} being larger than bulk, likely due to the influence of the substrate. Fig. 2(c) shows the rocking curves of the NbO (111) peak of the same films. The rocking curves consist of a narrow (N) main peak and a broad (B) peak, the latter of which we attribute to a disordered region at the Al_2O_3 -NbO interface. As T_G increases, the broad component becomes sharper, while the width of the narrow component remains similar. These changes can be captured by fitting the rocking curves using a Gaussian function for the narrow component and a squared Lorentzian function for the broad component [Supplemental Material, Fig. S3]. As shown in Fig. 2(d), the ratio of the full width at half maximum of the narrow component to that of the broad component increases as T_G increases, indicating improvements in crystal quality at elevated growth temperatures.

High T_G also helps to reproduce the low residual resistivity of NbO bulk crystals. Fig. 2(e) shows the temperature-dependent longitudinal resistivity of the same samples. Aside from the $T_G = 600$ °C sample, the temperature dependence of the resistivity is similar to bulk samples, with an approximately linear T dependence that flattens out due to residual disorder at low enough temperature [17, 24, 37]. As T_G increases, the temperature-dependent resistivity curve shifts downwards, which can be visualized by plotting the residual resistivity (ρ_0) at 1.7 K as a function of T_G [Fig. 2(f)]. ρ_0 of the lowest resistivity sample in this

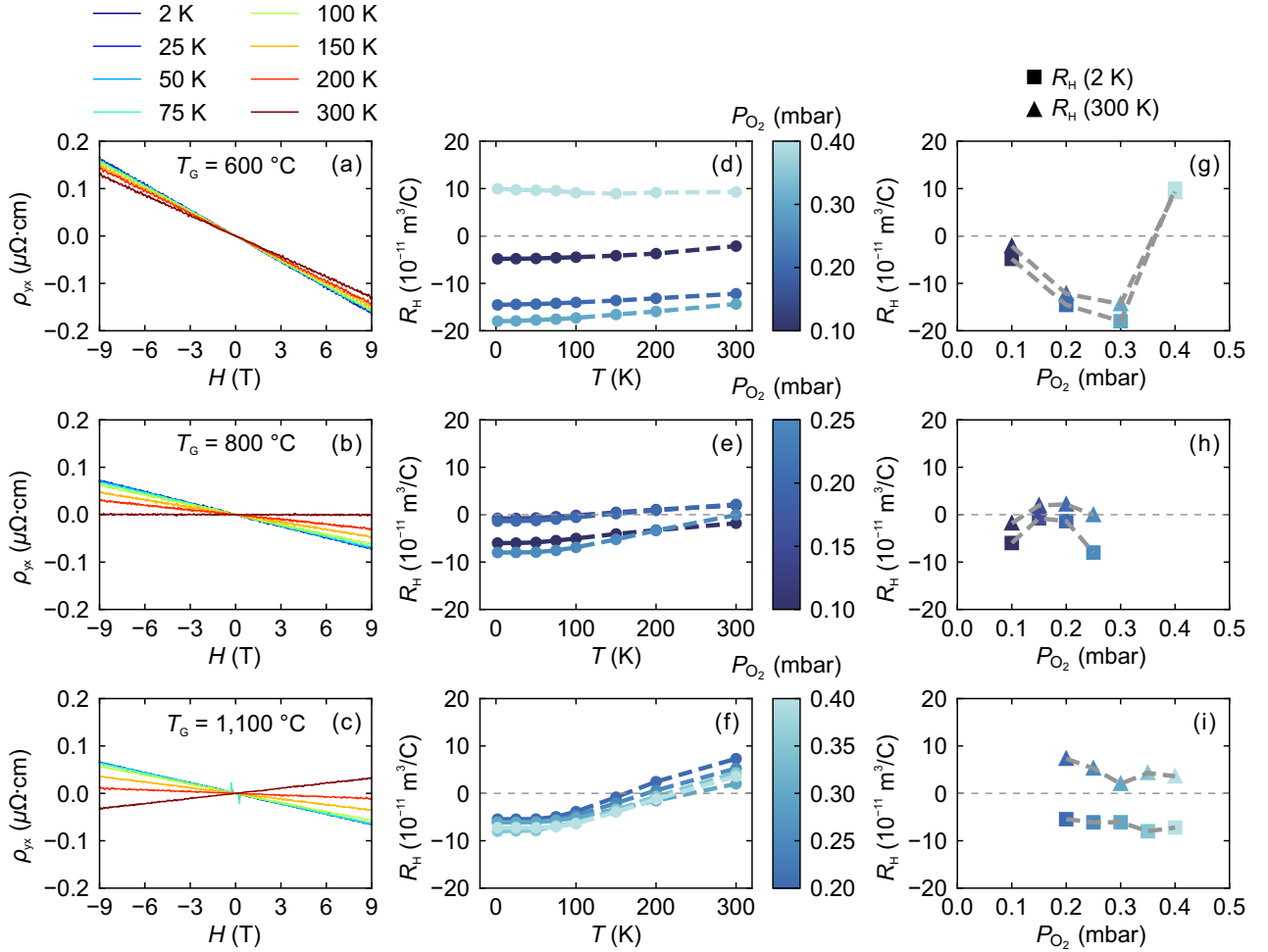


FIG. 3. Comparison of normal state transport properties of NbO films grown at $T_G = 600$ °C (top row), 800 °C (middle row), and 1100 °C (bottom row). (a-c) Hall resistivity at different temperatures of NbO films grown at the optimal P_{O_2} for each T_G . (d-f) Hall coefficient (R_H) versus temperature of samples grown at varying P_{O_2} . (g-i) R_H at 2 K (squares) and 300 K (triangles) of the same samples in (d-f). Dashed gray lines at $R_H = 0$ serve as a guide to the eye.

series ($T_G, P_{O_2} = (1100$ °C, 0.40 mbar) is 8 $\mu\Omega\cdot\text{cm}$, which is approaching the residual resistivity of 0.2 - 1.8 $\mu\Omega\cdot\text{cm}$ in bulk NbO [17, 24, 37]. In Figs. 2(g) and 2(h), ρ_0 and the residual resistivity ratio (RRR) have been mapped out in the T_G - P_{O_2} parameter space. As T_G increases, ρ_0 decreases and RRR increases, and there is little dependence of these properties on P_{O_2} .

We now turn our attention to the transport properties of NbO which have had no consensus in the literature. The temperature dependence of R_H has been reported for bulk NbO

samples with conflicting results. In one report, R_H changes sign from positive to negative as the measurement temperature increases [37]. In a different report, R_H is negative and increases with rising temperature for oxygen-deficient and stoichiometric NbO, but it switches sign from negative to positive for oxygen-rich NbO [24]. There has also been disagreement about the magnitude of T_c and its dependence on the O/Nb ratio. In Ref. [16], T_c reaches a maximum of 1.55 K at the stoichiometric composition and decreases at oxygen-deficient and oxygen-rich conditions. In Ref. [17], T_c shows a qualitatively similar dependence on the O/Nb ratio, but it reaches a maximum of 1.45 K at slightly oxygen-rich conditions. On the other hand, Ref. [15] reports a constant value of 1.38 K for stoichiometric and oxygen-rich conditions, and T_c rises sharply for oxygen-deficient conditions, which is attributed to the presence of Nb metal. Due to the effect of Nb impurities on the T_c of NbO, the magnitude of T_c is not a clear figure of merit in the NbO system.

In Figs. 3(a-c), we plot the symmetrized Hall resistivity at different temperatures for the $T_G = 600, 800$, and 1100 °C samples, which are grown at the optimal P_{O_2} for each T_G . The unsymmetrized Hall resistivity for these samples can be found in Supplemental Material, Fig. S4. The slope of the Hall resistivity is negative at all temperatures for the $T_G = 600$ and 800 °C samples, whereas the slope changes from negative at low temperatures to positive at high temperatures for the $T_G = 1100$ °C sample. The temperature dependence of R_H is illustrated in Figs. 3(d-f), where we compare NbO samples grown at fixed T_G and varying P_{O_2} . At $T_G = 600$ °C, R_H is either positive at all temperatures or negative at all temperatures, depending on the P_{O_2} . At $T_G = 800$ °C, the intermediate P_{O_2} samples have a negative R_H at low temperatures and positive R_H at high temperatures, whereas the low- and high- P_{O_2} samples exhibit a negative R_H at all temperatures. At $T_G = 1100$ °C, we observe the negative to positive temperature dependence of R_H , and the trend is consistent across all pressures. In Figs. 3(g-i), we plot the P_{O_2} dependence of R_H at 2 K (squares) and 300 K (triangles). The $T_G = 600$ °C series shows a non-monotonic dependence of R_H on P_{O_2} , first decreasing and then increasing as a function of P_{O_2} . The $T_G = 800$ °C series shows the opposite non-monotonic dependence, first increasing and then decreasing. In contrast, R_H of the $T_G = 1100$ °C series at each temperature is nearly constant as a function of P_{O_2} . We note that in all cases, R_H is similar in magnitude to bulk reports, but its dependence on P_{O_2} follows the trends observed in Ref. [24].

Fig. 4(a) shows the temperature-dependent resistivity of NbO samples grown at $T_G =$

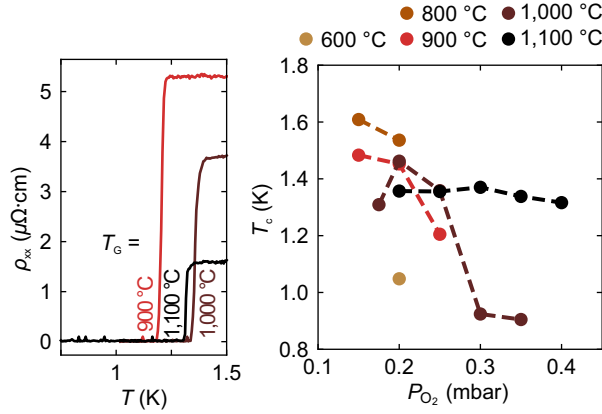


FIG. 4. Superconducting properties of NbO. (a) Temperature-dependent longitudinal resistivity of select samples grown at $T_G = 900, 1000, \text{ and } 1100 \text{ }^\circ\text{C}$ and the corresponding optimal P_{O_2} . (b) Superconducting transition temperature (T_c) of NbO films as a function of P_{O_2} for samples grown at varying T_G .

900, 1000, and 1100 $^\circ\text{C}$ and the optimal P_{O_2} . The transitions are all sharp, indicating good sample homogeneity. However, T_c , defined as the temperature at half resistance, does not show a clear dependence on T_G , so to gain insight we plot T_c as a function of P_{O_2} for the different T_G series [Fig. 4(b)]. For the $T_G = 800$ and 900 $^\circ\text{C}$ samples, T_c decreases slightly with increasing P_{O_2} . At $T_G = 1000 \text{ }^\circ\text{C}$, T_c increases initially and then decreases rapidly before flattening out above $P_{O_2} = 0.3 \text{ mbar}$. In contrast, there is little change in T_c for the $T_G = 1100 \text{ }^\circ\text{C}$ samples as a function of P_{O_2} .

IV. DISCUSSION

Our results establish that R_H and T_c of NbO vary dramatically with growth parameters, and the beneficial effects of T_G on the quantifiable figures of merit indicate that thermal activation is indispensable to realizing the desirable properties of NbO films. Although 600~1000 $^\circ\text{C}$ is a conventional temperature range for most thin film deposition techniques, the ideal growth temperature for the epitaxial Nb-O system exceeds this window due to the refractory nature of Nb. To further this discussion, we consider a simple model of the Nb-O system in which the oxygen content varies, resulting in non-stoichiometric NbO_{1+x} ($-0.02 \leq x \leq 0.02$). When the amount of deviation is above that which the NbO phase can

tolerate, the coexistence of NbO and a secondary phase occurs. These secondary phases are Nb on the oxygen-deficient side and NbO₂ on the oxygen-rich side. The manner in which non-stoichiometry and phase coexistence influence the electrical properties are discussed below.

The superconductivity of NbO is likely of conventional origin [15], so T_c is positively correlated with the Debye temperature (Θ_D), the density of states at the Fermi level (N_0), and the electron-phonon interaction (V_{ph}) [38]. Within the NbO region, we expect an electron doping effect (Fermi level rise) as oxygen content decreases. DFT calculations show that N_0 increases as the Fermi level rises [19, 22], which accordingly should influence T_c . While conventional superconductors are generally tolerant to non-magnetic crystalline disorder, structural non-uniformity can suppress T_c and/or widen the superconducting transition [see Supplemental Material, Fig. S5 for transitions]. Combining the effects of N_0 and crystallinity, we expect T_c to be maximized at a slightly sub-stoichiometric condition. Further deviating from the stoichiometric composition, in the Nb-rich region, T_c has been reported to rapidly increase due to the inclusion of Nb, which has a much higher T_c (9.25 K) than NbO [39]. In the NbO₂-containing region, T_c is expected to be moderately suppressed as NbO₂ is not superconducting, resulting in a non-uniform superconducting landscape where pairing is suppressed via proximity to a normal material.

Turning to bulk transport properties, R_H is an algebraic sum of the individual contributions of each carrier, which are of different sign [20]. As NbO contains many electron and hole pockets near the Fermi level, shifting the Fermi level changes the relative filling of the bands. According to the band structure, NbO becomes hole-dominated as the Fermi level is decreased (oxygen content is increased) and electron-dominated as the Fermi level is increased (oxygen content is decreased). Therefore, in the NbO_{1+x} region, R_H should become more positive (negative) in oxygen-rich (deficient) conditions. As for the defect phases, R_H is reported to be positive for both Nb [40, 41], and NbO₂ [42, 43].

These trends largely agree with our observations in the $T_G = 1000$ °C sample series. In the NbO_{1+x} region, T_c is maximized at a pressure lower than the structurally optimal P_{O_2} , while it decreases on either side of this pressure. When P_{O_2} is further decreased towards the Nb-rich region, T_c sharply increases [Supplemental Material, Fig. S6]. R_H follows a similar trend as a function of P_{O_2} [Supplemental Material, Fig. S7], which is likely due to the competing dominance of different carrier types in the various phase regions.

In the low T_G samples, these trends are complicated by the lack of sharp phase boundaries between Nb and NbO [Fig. 1(f)]. In the Nb-O system, we are able to detect Nb via electrical but not structural measurements [Supplemental Material, Fig. S6]. We can infer that this non-detectable Nb is more pervasive in the low- T_G films, given the blurring of the phase boundaries and the amorphous nature of Nb on Al_2O_3 (0001) at these temperatures. We clearly resolve that T_c increases as we reduce P_{O_2} , but it is difficult to distinguish the effects of Nb impurities and the NbO Fermi level change. R_H does not show a clear dependence on T_G or P_{O_2} , and interpretation is difficult due to the extrinsic effects of poor crystallinity and phase coexistence. For the sake of completeness we have also measured T_c and R_H of amorphous and crystalline Nb films [Supplemental Material, Fig. S8].

We finally discuss the role of high temperature synthesis in NbO, and, more generally, in reduced refractory oxides. First, as a basic means of improving adatom mobility and sample homogeneity, high T_G (> 1000 °C) enables superior structural and electrical properties (evidenced by ρ_0 and RRR). Second, it facilitates the reproducible synthesis of NbO within the thermally-activated epitaxy regime where the magnitude of T_c , and the sign and magnitude of R_H at different temperatures, are consistent for a finite range of P_{O_2} -variation. This thermally-activated epitaxy closely resembles reported self-limited growth mechanisms that yield optimal material properties within a wide growth window. Examples include the adsorption-controlled growth of GaAs [44] and SrTiO_3 [45], and the diffusion-controlled growth of the Ti-O system [46].

V. CONCLUSION

We observed competing growth mechanisms in the synthesis of the Nb-O system, driven by kinetics at low temperatures and thermodynamics at high temperatures. Ultra-high growth temperature was a key to realizing excellent crystal quality, superior transport properties, and reproducible synthesis. We have demonstrated improved quality of NbO at ultra-high temperatures and a growth window yielding consistent physical properties. As such, we propose the following prototypical properties of NbO: (1) R_H that is negative at low temperatures and positive at high temperatures, and (2) T_c of 1.32-1.37 K. Our study highlights the importance of thermal activation in the thin film synthesis of refractory metal compounds across large thermodynamic windows.

ACKNOWLEDGMENTS

We thank Bharat Jalan for his valuable comments. We acknowledge funding provided by the Gordon and Betty Moore Foundation’s EPiQS Initiative (Grant number GBMF10638), the Institute for Quantum Information and Matter, a NSF Physics Frontiers Center (NSF Grant PHY-2317110), and the AWS Center for Quantum Computing through a sponsored research initiative. This research was carried out at the Jet Propulsion Laboratory and the California Institute of Technology under a contract with the National Aeronautics and Space Administration and funded through the President’s and Director’s Research & Development Fund Program.

- [1] W. Witczak-Krempa, G. Chen, Y. B. Kim, and L. Balents, Correlated Quantum Phenomena in the Strong Spin-Orbit Regime, [Annual Review of Condensed Matter Physics](#) **5**, 57 (2014).
- [2] S. Manzeli, D. Ovchinnikov, D. Pasquier, O. V. Yazyev, and A. Kis, 2D transition metal dichalcogenides, [Nat Rev Mater](#) **2**, 17033 (2017).
- [3] N. P. Armitage, E. J. Mele, and A. Vishwanath, Weyl and Dirac semimetals in three-dimensional solids, [Rev. Mod. Phys.](#) **90**, 015001 (2018).
- [4] B. Yan and C. Felser, Topological Materials: Weyl Semimetals, [Annual Review of Condensed Matter Physics](#) **8**, 337 (2017).
- [5] J. G. Rau, E. K.-H. Lee, and H.-Y. Kee, Spin-Orbit Physics Giving Rise to Novel Phases in Correlated Systems: Iridates and Related Materials, [Annual Review of Condensed Matter Physics](#) **7**, 195 (2016).
- [6] M. N. Ali, J. Xiong, S. Flynn, J. Tao, Q. D. Gibson, L. M. Schoop, T. Liang, N. Haldolaarachchige, M. Hirschberger, N. P. Ong, and R. J. Cava, Large, non-saturating magnetoresistance in WTe₂, [Nature](#) **514**, 205 (2014).
- [7] C. Shekhar, A. K. Nayak, Y. Sun, M. Schmidt, M. Nicklas, I. Leermakers, U. Zeitler, Y. Skourski, J. Wosnitza, Z. Liu, Y. Chen, W. Schnelle, H. Borrman, Y. Grin, C. Felser, and B. Yan, Extremely large magnetoresistance and ultrahigh mobility in the topological Weyl semimetal candidate NbP, [Nature Phys](#) **11**, 645 (2015).

[8] X. Huang, Observation of the Chiral-Anomaly-Induced Negative Magnetoresistance in 3D Weyl Semimetal TaAs, *Phys. Rev. X* **5**, [10.1103/PhysRevX.5.031023](https://doi.org/10.1103/PhysRevX.5.031023) (2015).

[9] C.-L. Zhang, S.-Y. Xu, I. Belopolski, Z. Yuan, Z. Lin, B. Tong, G. Bian, N. Alidoust, C.-C. Lee, S.-M. Huang, T.-R. Chang, G. Chang, C.-H. Hsu, H.-T. Jeng, M. Neupane, D. S. Sanchez, H. Zheng, J. Wang, H. Lin, C. Zhang, H.-Z. Lu, S.-Q. Shen, T. Neupert, M. Zahid Hasan, and S. Jia, Signatures of the Adler–Bell–Jackiw chiral anomaly in a Weyl fermion semimetal, *Nat Commun* **7**, 10735 (2016).

[10] H.-Z. Lu and S.-Q. Shen, Weak antilocalization and localization in disordered and interacting Weyl semimetals, *Phys. Rev. B* **92**, 035203 (2015).

[11] F. Arnold, C. Shekhar, S.-C. Wu, Y. Sun, R. D. dos Reis, N. Kumar, M. Naumann, M. O. Ajeesh, M. Schmidt, A. G. Grushin, J. H. Bardarson, M. Baenitz, D. Sokolov, H. Borrmann, M. Nicklas, C. Felser, E. Hassinger, and B. Yan, Negative magnetoresistance without well-defined chirality in the Weyl semimetal TaP, *Nat Commun* **7**, 11615 (2016).

[12] J. Yang, W. L. Zhen, D. D. Liang, Y. J. Wang, X. Yan, S. R. Weng, J. R. Wang, W. Tong, L. Pi, W. K. Zhu, and C. J. Zhang, Current jetting distorted planar Hall effect in a Weyl semimetal with ultrahigh mobility, *Phys. Rev. Materials* **3**, 014201 (2019).

[13] B. Q. Lv, T. Qian, and H. Ding, Experimental perspective on three-dimensional topological semimetals, *Rev. Mod. Phys.* **93**, 025002 (2021).

[14] P. Goswami, Axial anomaly and longitudinal magnetoresistance of a generic three-dimensional metal, *Phys. Rev. B* **92**, [10.1103/PhysRevB.92.075205](https://doi.org/10.1103/PhysRevB.92.075205) (2015).

[15] J. K. Hulm, C. K. Jones, R. A. Hein, and J. W. Gibson, Superconductivity in the TiO and NbO systems, *J Low Temp Phys* **7**, 291 (1972).

[16] A. M. Okaz and P. H. Keesom, Specific heat and magnetization of the superconducting monoxides: NbO and TiO, *Phys. Rev. B* **12**, 4917 (1975).

[17] E. R. Pollard, *Electronic Properties of Niobium Monoxide*, Ph.D. thesis, Massachusetts Institute of Technology (1968).

[18] J. K. Burdett and T. Hughbanks, Niobium oxide (NbO) and titanium oxide (TiO): A study of the structural and electronic stability of structures derived from rock salt, *J. Am. Chem. Soc.* **106**, 3101 (1984).

[19] E. Wimmer, K. Schwarz, R. Podloucky, P. Herzig, and A. Neckel, The effect of vacancies on the electronic structure of NbO, *Journal of Physics and Chemistry of Solids* **43**, 439 (1982).

[20] W. Wahnsiedler, Energy Band Structure and Electronic Transport Properties of Niobium Monoxide, *Journal of Solid State Chemistry* **49**, 195 (1983).

[21] H. Aoki, Y. Asada, T. Hatano, K. Ogawa, A. Yanase, and M. Koiwa, Fermi surface of NbO, *J Low Temp Phys* **81**, 19 (1990).

[22] A. K. Efimenko, N. Hollmann, K. Hoefer, J. Weinen, D. Takegami, K. K. Wolff, S. G. Altdendorf, Z. Hu, A. D. Rata, A. C. Komarek, A. A. Nugroho, Y. F. Liao, K.-D. Tsuei, H. H. Hsieh, H.-J. Lin, C. T. Chen, L. H. Tjeng, and D. Kasinathan, Electronic signature of the vacancy ordering in NbO (Nb_3O_3), *Phys. Rev. B* **96**, 195112 (2017).

[23] G. Chandrashekhar, J. Moyo, and J. Honig, Electrical resistivity of NbO, *Journal of Solid State Chemistry* **2**, 528 (1970).

[24] J. M. Honig, W. E. Wahnsiedler, and P. C. Eklund, Electrical properties of NbO in high magnetic fields, *Journal of Solid State Chemistry* **6**, 203 (1973).

[25] J. R. Kim, S. Glotzer, E. Krysko, M. R. Barone, J. Kim, S. Salmani-Rezaie, A. Llanos, and J. Falson, Superconducting Vacancy-Ordered Rock-Salt NbO Films, *Chem. Mater.* [10.1021/acs.chemmater.5c01074](https://doi.org/10.1021/acs.chemmater.5c01074) (2025).

[26] W. Martienssen and H. Warlimont, *Springer Handbook of Condensed Matter and Materials Data* (Springer Science & Business Media, 2006).

[27] F. C. Campbell, *Elements of Metallurgy and Engineering Alloys* (ASM International, 2008).

[28] E. M. Savitskii, *Physical Metallurgy of Refractory Metals and Alloys* (Springer Science & Business Media, 2012).

[29] E. K. Storms, *The Refractory Carbides* (Elsevier, 1967).

[30] L. Toth, *Transition Metal Carbides and Nitrides* (Elsevier, 1971).

[31] H. O. Pierson, *Handbook of Refractory Carbides and Nitrides: Properties, Characteristics, Processing and Applications* (William Andrew, 1996).

[32] M. W. Chase, NIST-JANAF Thermochemical Tables, Fourth Edition, *J. Phys. Chem. Ref. Data*, Monograph 9 , 1 (1998).

[33] K. T. Jacob, C. Shekhar, M. Vinay, and Y. Waseda, Thermodynamic Properties of Niobium Oxides, *J. Chem. Eng. Data* **55**, 4854 (2010).

[34] S.-L. Shang, S. Lin, M. C. Gao, D. G. Schlom, and Z.-K. Liu, Ellingham diagrams of binary oxides, *APL Materials* **12**, 081110 (2024).

[35] H. J. T. Ellingham, Transactions and Communications, *J. Soc* **63**, 125 (1944).

[36] C. McLintock and J. Stringer, The pressure dependence of the linear oxidation of niobium in the temperature range 450°–1050°C, *Journal of the Less Common Metals* **5**, 278 (1963).

[37] W. W. Schulz, L. Forro, C. Kendziora, R. Wentzcovitch, D. Mandrus, L. Mihaly, and P. B. Allen, Band structure and electronic transport properties of the superconductor NbO, *Phys. Rev. B* **46**, 14001 (1992).

[38] J. Bardeen, L. N. Cooper, and J. R. Schrieffer, Theory of Superconductivity, *Phys. Rev.* **108**, 1175 (1957).

[39] D. K. Finnemore, T. F. Stromberg, and C. A. Swenson, Superconducting Properties of High-Purity Niobium, *Phys. Rev.* **149**, 231 (1966).

[40] T. G. Berlincourt, Hall Effect, Resistivity, and Magnetoresistivity of Th, U, Zr, Ti, and Nb, *Phys. Rev.* **114**, 969 (1959).

[41] W. R. Cox, D. J. Hayes, and F. R. Brotzen, Temperature Dependence of the Hall Effect and Resistivity in Single Crystals of Mo and Nb and of Mo-Rich-Re, Mo-Nb, and Nb-Rich-Zr Alloys, *Phys. Rev. B* **7**, 3580 (1973).

[42] G. Bélanger, J. Destry, G. Perluzzo, and P. M. Raccah, Electron Transport in Single Crystals of Niobium Dioxide, *Can. J. Phys.* **52**, 2272 (1974).

[43] Y. Sakai, N. Tsuda, and T. Sakata, Electrical Properties of Semiconducting NbO₂, *J. Phys. Soc. Jpn.* **54**, 1514 (1985).

[44] J. R. Arthur, Jr., Interaction of Ga and As₂ Molecular Beams with GaAs Surfaces, *J. Appl. Phys.* **39**, 4032 (1968).

[45] B. Jalan, P. Moetakef, and S. Stemmer, Molecular beam epitaxy of SrTiO₃ with a growth window, *Appl. Phys. Lett.* **95**, 032906 (2009).

[46] J. R. Kim, S. Glotzer, A. Llanos, S. Salmani-Rezaie, and J. Falson, High-Temperature Diffusion Enabled Epitaxy of the Ti–O System, *Advanced Materials* **37**, 2413447 (2025).

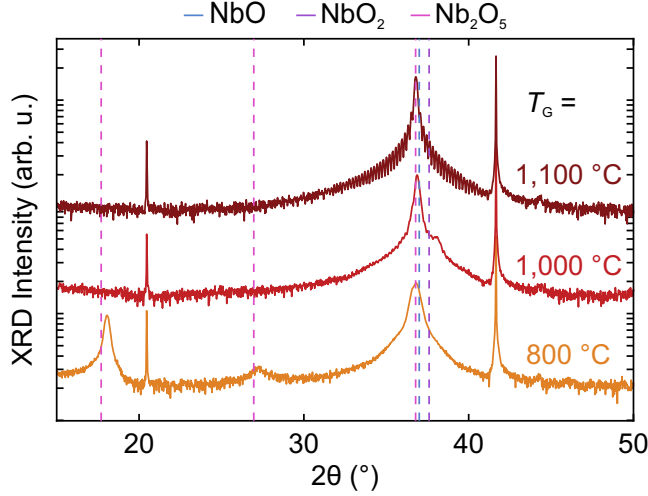


FIG. S1. Identification of impurity phases in the Nb-O system. Wide-range XRD 2θ - ω scans of Nb-O films grown at $P_{O_2} = 0.4$ mbar and varying T_G . Dashed lines correspond to the bulk peak positions for NbO (blue), rutile NbO₂ (purple), and H-Nb₂O₅ (pink). As there are numerous polymorphs and crystal structures of Nb₂O₅, it is difficult to unambiguously assign a phase.

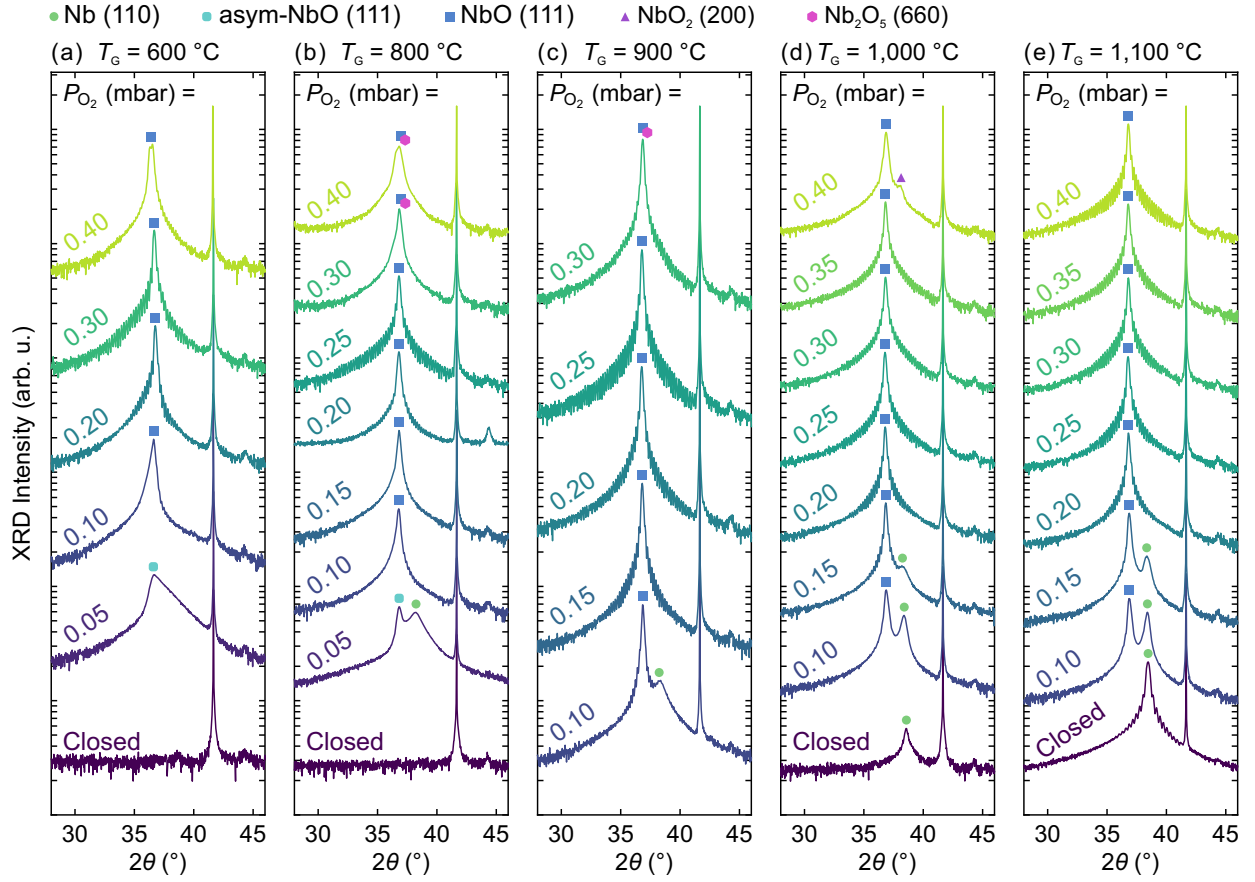


FIG. S2. Narrow-range XRD 2θ - ω scans of Nb-O films grown at varying P_{O_2} and (a) $T_G = 600$ °C, (b) $T_G = 800$ °C, (c) $T_G = 900$ °C, (d) $T_G = 1000$ °C, and (e) $T_G = 1100$ °C. Symbols correspond to body-centered-cubic Nb (green circle), asymmetric NbO (cyan rounded square), single-phase, single-crystal NbO (filled blue square), rutile NbO₂ (purple triangle), and Nb₂O₅ (pink hexagon).

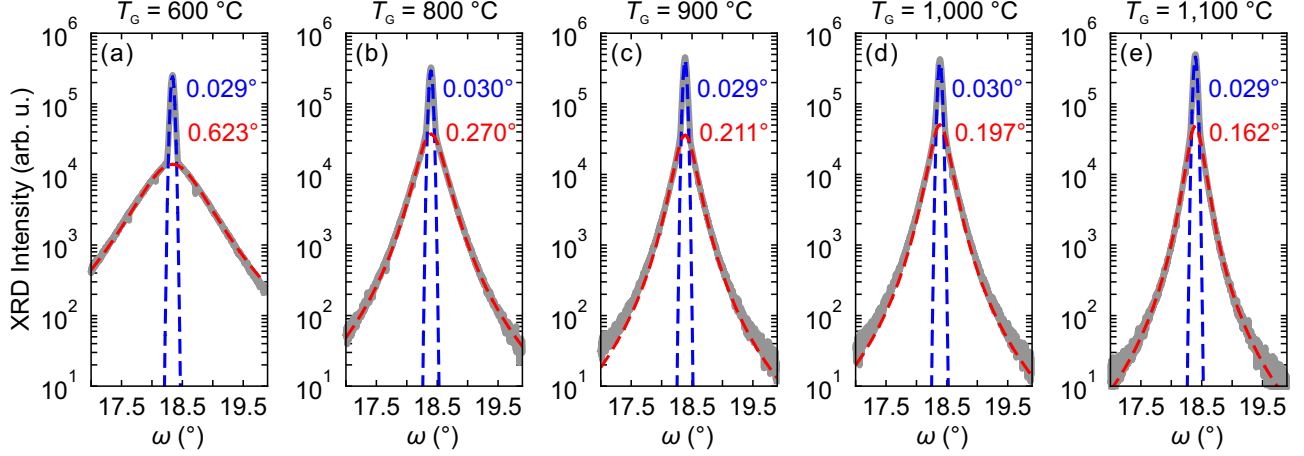


FIG. S3. Fits of the NbO (111) rocking curves for the samples shown in Fig. 2. Samples were grown at the optimal P_{O_2} for each T_G and (a) $T_G = 600\text{ }^\circ\text{C}$, (b) $T_G = 800\text{ }^\circ\text{C}$, (c) $T_G = 900\text{ }^\circ\text{C}$, (d) $T_G = 1000\text{ }^\circ\text{C}$, and (e) $T_G = 1100\text{ }^\circ\text{C}$. The curves were fitted using a Gaussian function (blue) and a squared Lorentzian function (red). The full width at half maximum values of the Gaussian and squared Lorentzian components are displayed in blue and red text.

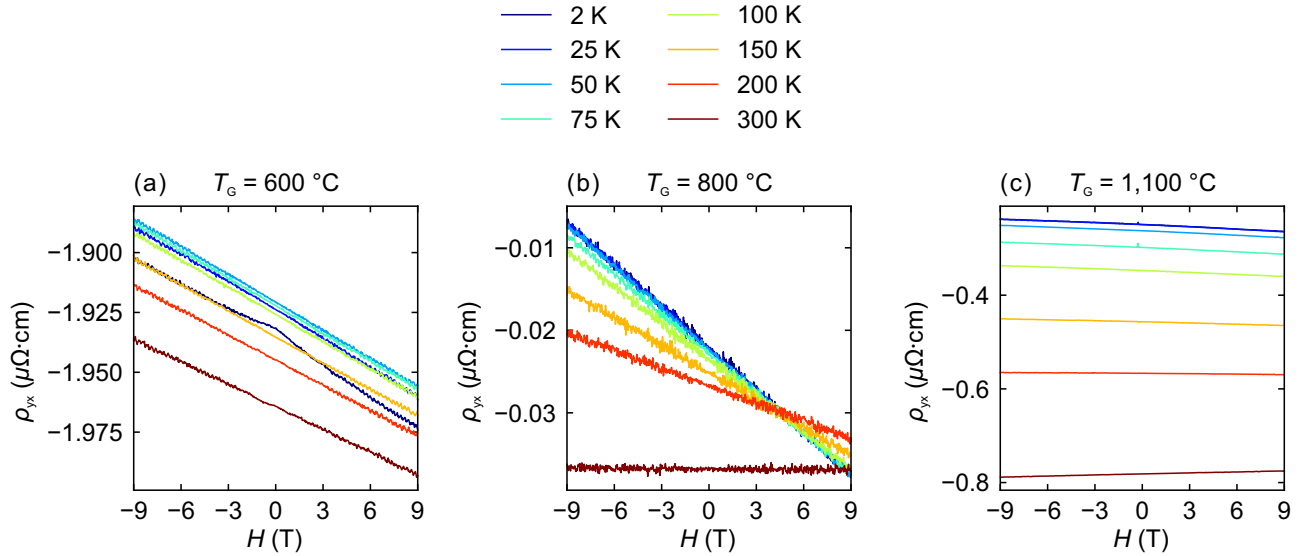


FIG. S4. Unsymmetrized Hall resistivity for the NbO samples shown in Fig. 3. Samples were grown at the optimal P_{O_2} for each T_G and (a) $T_G = 600\text{ }^\circ\text{C}$, (b) $T_G = 800\text{ }^\circ\text{C}$, and (c) $T_G = 1,100\text{ }^\circ\text{C}$.

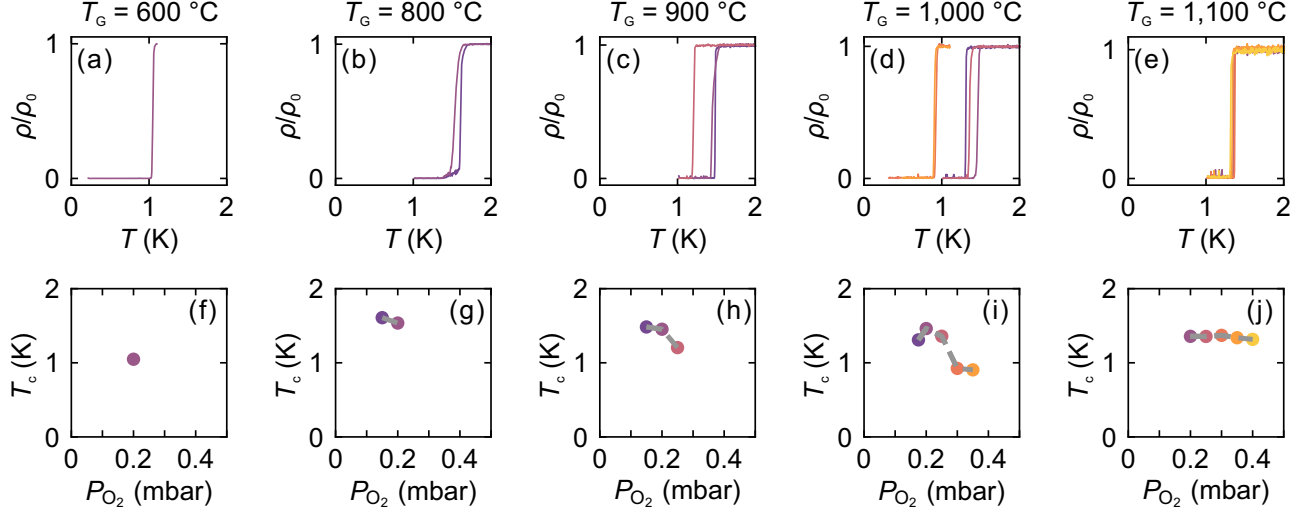


FIG. S5. Superconducting transitions of NbO films grown at $T_G = 600$ °C (first column), $T_G = 800$ °C (second column), $T_G = 900$ °C (third column), $T_G = 1000$ °C (fourth column), and $T_G = 1100$ °C (fifth column). (a-e) Temperature-dependent longitudinal resistivity at various P_{O_2} and (f-j) T_c as a function of P_{O_2} .

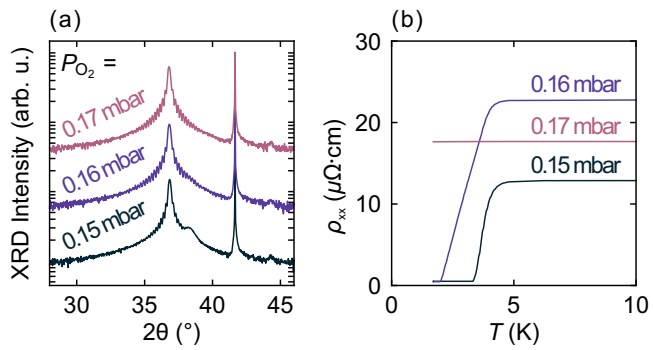


FIG. S6. Narrow-range P_{O_2} -dependent growths of Nb-O films grown at $T_G = 1000$ °C. (a) XRD 2θ - ω scans and (b) temperature-dependent longitudinal resistivity.

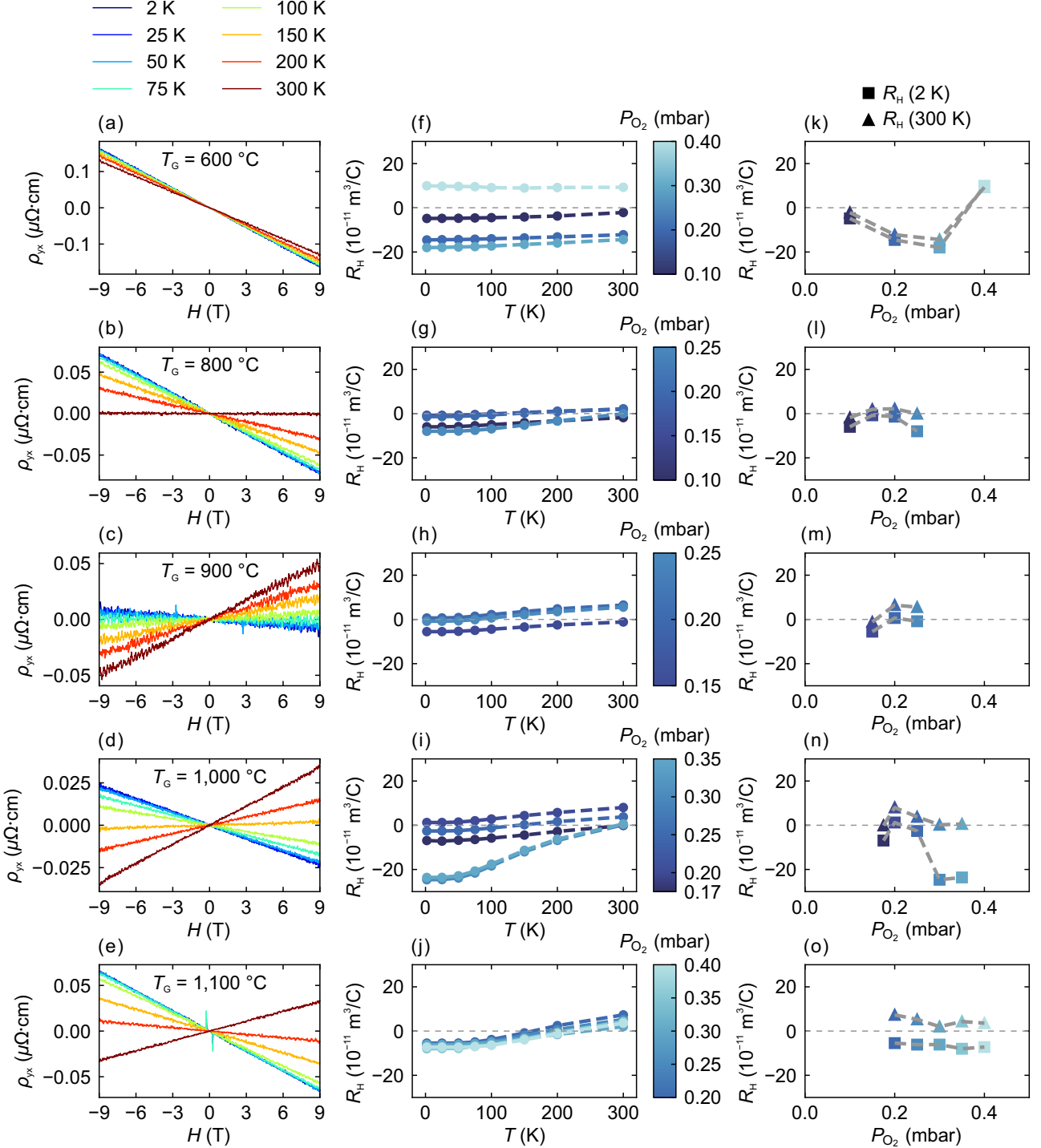


FIG. S7. Comparison of transport properties of NbO films grown at $T_G = 600\text{ }^{\circ}\text{C}$ (first row), $T_G = 800\text{ }^{\circ}\text{C}$ (second row), $T_G = 900\text{ }^{\circ}\text{C}$ (third row), $T_G = 1000\text{ }^{\circ}\text{C}$ (fourth row), and $T_G = 1100\text{ }^{\circ}\text{C}$ (fifth row). (a-e) Hall resistivity at different temperatures of NbO films grown at the optimal P_{O_2} for each T_G . (f-j) Hall coefficient (R_{H}) versus temperature of samples grown at varying P_{O_2} . (k-o) R_{H} at 2 K (squares) and 300 K (triangles) of the same samples. Dashed gray lines at $R_{\text{H}} = 0$ serve as a guide to the eye.

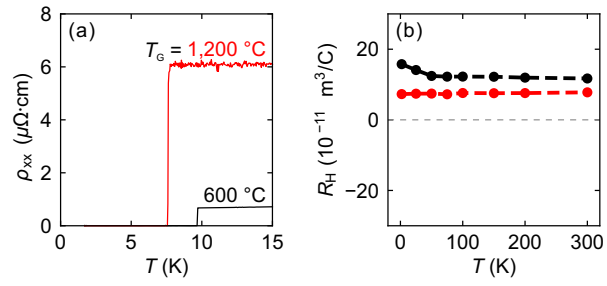


FIG. S8. Transport measurements of an amorphous Nb film grown at $(T_G, P_{O_2}) = (600 \text{ } ^\circ\text{C}, \text{ "Closed"})$ (black) and a crystalline Nb film grown at $(T_G, P_{O_2}) = (1200 \text{ } ^\circ\text{C}, \text{ "Closed"})$ (red). a) Temperature-dependent longitudinal resistivity. (b) R_H versus temperature. Dashed gray line at $R_H = 0$ serves as a guide to the eye.